Probing Local Electromechanical Effects in Highly Conductive Electrolytes

Nina Balke,[†,*] Alexander Tselev,[†] Thomas M. Arruda,[†] Stephen Jesse,[†] Ying-Hao Chu,[‡] and Sergei V. Kalinin[†]

[†]Center for Nanophase Materials Sciences, Oak Ridge National Laboratory, Oak Ridge, Tennessee 37831, United States and [‡]Department of Materials Science and Engineering, National Chiao Tung University, Hsinchu 30010, Taiwan

ABSTRACT The functionality of a variety of materials and devices is strongly coupled with electromechanical effects which can be used to characterize their functionality. Of high interest is the investigation of these electromechanical effects on the nanoscale which can be achieved by using scanning probe microscopy. Here, an electrical bias is applied locally to the scanning probe tip, and the mechanical sample response is detected. In some applications with electromechanical phenomena, such as energy storage or for biological samples, a liquid environment is required to provide full functionality and sample stability. However, electromechanical sample characterization has mostly been applied in air or under vacuum due to the difficulties of applying local electric fields in a conductive environment. Here, we present a detailed study of piezoresponse force microscopy of ferroelectric samples in liquid environments as a model system for electromechanical effects in general. The ionic strength of the liquid is varied, and possibilities and limitations of the technique are explored. Numerical simulations are used to explain the observed phenomena and used to suggest strategies to work in liquid environments with high ionic strength.

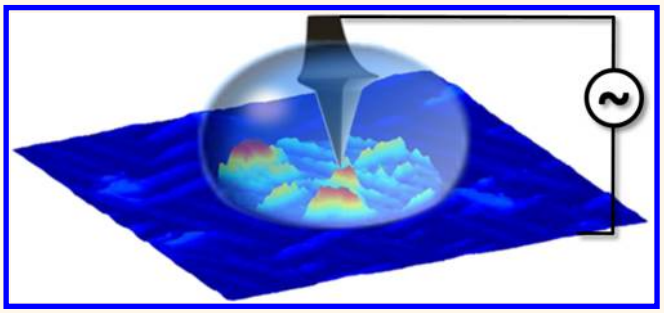

KEYWORDS: scanning probe microscopy · liquid · ferroelectrics · electromechanics · piezoresponse force microscopy

Electromechanical phenomena defined as a change in strain or stress in response to an electrical stimulus are manifested in a broad range of materials and systems ranging from physical such as ferro- and piezoelectrics,[1,2] electrochemical ionic systems including batteries,[3] fuel cells,[4] supercapacitors,[5] and more complex macromolecular[6,7] and biological[8] systems. In many cases, electromechanical responses are ultimately related to functionality, including lifetimes and stability of batteries and fuel cells. At the same time, electromechanical coupling probed on the nanoscale opens the window toward understanding the elementary mechanisms underpinning these systems.

The most prominent example is ferroelectric materials, broadly used for applications such as ferroelectric random access memories (FeRAM)[9] and microelectromechanical systems (MEMS).[10] With scanning probe microscopy (SPM) techniques, it is possible to use electromechanics as the basis for high-resolution imaging to investigate the nanoscale functionality in these systems. For ferroelectrics, the electromechanical response of the sample to a varying ac field, as a result of the piezoelectric effect, can be used to detect domain orientations and local piezoelectric coefficients. This technique is referred to as piezoresponse force microscopy (PFM).[11−19] Similar approaches can be used for ferroelectric polymers[20,21] and biological systems.[22−25]

Other examples of the systems with strong electromechanical coupling are ionic systems including materials for Li-ion batteries and fuel cells. Here, the volume change is induced by a bias-driven change in ionic concentration in the material and the strong coupling between ionic concentration and molar volume.[26] The indirect detection of ion flows through strain has been utilized in electrochemical strain microscopy (ESM),[27,28] based on the same excitation and detection principles as PFM. However, PFM or ESM has been performed almost exclusively in air.

* Address correspondence to balken@ornl.gov.

Received for review August 24, 2012 and accepted October 29, 2012.

Published online October 29, 2012
10.1021/nn3038868

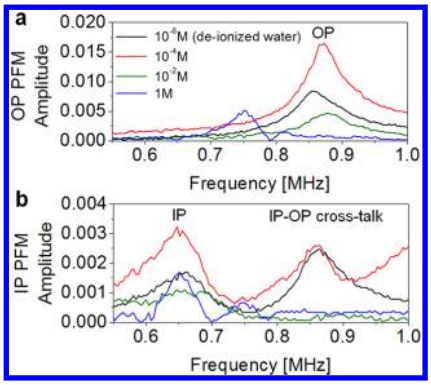

Figure 1. (a) OP and (b) IP PFM amplitude as a function of excitation frequency for Na_2SO_4 electrolytes with molarities from 10^{-6} to 1 M.

Due to the large interest in electromechanical studies of ionic and biological systems, it is of great interest to advance electromechanical characterization techniques into the liquid environment to provide spatially resolved information in native environments.

Recently, we have shown that the imaging and manipulation of ferroelectric domains can be performed in deionized water as a liquid medium using single and multiple frequency contact resonance PFM.[29] Ferroelectrics were chosen as a model system for electromechanical systems in general and can be easily transferred to ionic systems.[30−32] However, for ionic systems, the liquid environment consists of high concentration electrolytes, typically of the order of 1 M, which are much more ionically conductive than deionized water. This brings additional challenges to the electromechanical characterization in the liquid environment since the conductivity of the liquid strongly affects the electrical potential around the biased SPM tip and can possibly limit the application of electromechanical characterization in liquid to energy storage materials. Therefore, it is important to study electromechanical effects in highly conductive liquids and determine its application limits.

RESULTS

Here, we perform PFM on ferroelectric $BiFeO_3$ (BFO) as a model system in Na_2SO_4 electrolyte with molarities ranging from 10^{-6} M (deionized water) to 1 M. The electrolyte was chosen based on compatibility with the SPM environment. We compare the experiments with numerical modeling of the electrical potential around the biased SPM tip as a function of electrolyte conductivity using finite element (FE) analysis software COMSOL. Figure 1 shows the out-of-plane (OP) and in-plane (IP) PFM amplitude between 550 kHz and 1 MHz. It can be seen that the OP contact resonance peak is around 870 kHz and shifts strongly toward lower frequencies for 1 M Na_2SO_4. At the OP resonance frequency, the IP PFM amplitude shows a resonance as well for lower molarities. This is due to a cross-talk between the OP and IP signal. This resonance peak cannot be used to image IP PFM. However, the IP PFM signal has an independent resonance peak at 650 kHz for all molarities. Because this peak does not shift with increasing concentration, single frequency IP PFM is performed at 650 kHz in the following PFM measurements.

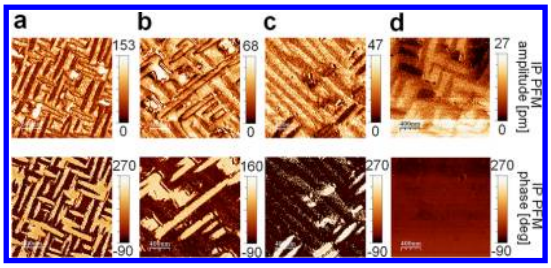

Figure 2. IP PFM images for BFO measured in a liquid environment at 650 kHz in (a) 10^{-6} M Na_2SO_4, (b) 10^{-4} M Na_2SO_4, (c) 10^{-2} M Na_2SO_4, and (d) 1 M Na_2SO_4.

Figure 2 displays the IP PFM images of BFO for electrolytes consisting of 10^{-6}, 10^{-4}, 10^{-2}, and 1 M Na_2SO_4 solutions measured at 650 kHz. The characteristic stripe-like domain pattern can be identified for all concentrations up to 1 M. Here, the observed signal is 2 orders of magnitude higher than what has been reported previously with NaCl electrolytes.[30] This can be mainly attributed to the higher contact resonance frequencies above 650 kHz for the cantilevers used in this study, which allows measurement at higher molarities due to a reduced field screening effect at higher ac frequencies. However, the images become less clear, that is, a decrease in spatial resolution, in addition of the loss of the PFM phase information at 1 M Na_2SO_4. In fact, both the amplitude of the electromechanical response and spatial resolution decrease until no meaningful images can be obtained.

Numerical Modeling. To understand the observations in more detail, let us consider the electrical behavior of the tip−sample system immersed in a conducing electrolyte with a relative dielectric constant ε_{el} and specific conductivity σ_{el}. The tip apex is in contact with a dielectric film, whose relative permittivity is ε_{film}. At the frequencies used for detection of the piezoresponse, the double layer at the tip−electrolyte interface serves as a capacitive short, and therefore its effects can be ignored. In this approximation, the electrolyte can be modeled as a lossy dielectric; that is, its presence can be described by a lumped element circuit consisting of a parallel resistor and capacitor. The dielectric film can be modeled as a capacitor in series with electrolyte. To take into account the conical shape of the tip and the distributed nature of the system, we divide the tip cone surface and the film surface into narrow rings. A ring on the tip surface corresponds to a ring on the film surface so that the two rings are connected by electric field lines.

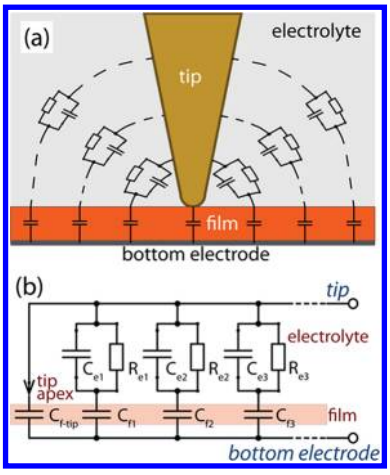

Figure 3. (a) Schematic illustrating electrical behavior of the tip−sample system with a tip in contact with a dielectric film immersed into an electrolyte solution. The presence of the double layer at the tip−electrolyte interface is ignored. (b) Equivalent distributed lumped element circuit of the tip−sample system.

As illustrated in Figure 3a, the volumes of the electrolyte and the film corresponding to a pair of such rings can be described by a $C_{fn} + C_{eln} \parallel R_{eln}$ circuit, where the plus sign denotes connection in series and "∥" means connection in parallel. Figure 2b displays the resulting circuit, where $C_{fn} \approx C_{f(n+1)}$, $C_{eln} > C_{el(n+1)}$, and $R_{eln} < R_{el(n+1)}$. Capacitance of the tip apex at the contact with the films is accounted by a capacitor $C_{f\text{-}tip}$. Now we note that the localization of the piezoresponse will be achieved if the voltage applied to the tip, V_{tip}, drops through the film only under the tip−film contact (through the capacitor $C_{f\text{-}tip}$); everywhere else it must drop through the electrolyte. Each partial circuit $C_{fn} + C_{eln} \parallel R_{eln}$ is a voltage divider with input voltage V_{tip} and an output voltage V_{fn} equal to the voltage across the capacitor C_{fn}. The relation between V_{tip} and a V_{fn} for a given n can be written as

$$\frac{|V_{fn}|}{|V_{tip}|} = \sqrt{\frac{G_{eln}^2 + C_{eln}^2\omega^2}{G_{eln}^2 + (C_{eln}+C_{fn})^2\omega^2}} = \sqrt{\frac{\tan^2\delta_{el} + 1}{\tan^2\delta_{el} + \left(1+\frac{C_{fn}}{C_{eln}}\right)^2}} \quad (1)$$

where $\omega = 2\pi f$ is angular frequency, $G_{eln} = 1/R_{eln}$, ε_0 is the dielectric constant of vacuum, and $\tan\delta_{el}$ is the electrolyte loss tangent defined as $\tan\delta_{el} = \sigma_{el}/(\omega\varepsilon_0\varepsilon_{el})$. The transition from the lumped element values to conductivity and dielectric constant of the electrolyte is possible if the widths of the rings used to define partial C_{eln} and R_{eln} are sufficiently small. Then, each $C_{eln}-R_{eln}$ pair may be treated as a parallel-plate capacitor, and consequently, the loss tangent can be expressed through a partial capacitance and conductance as $\tan\delta_{el} = G_{eln}/(\omega C_{eln})$. This fact is used in the last part of eq 1.

As is seen from eq 1, if $\tan\delta_{el} \ll 1$, then

$$\frac{|V_{fn}|}{|V_{tip}|} \approx \frac{C_{eln}}{C_{eln} + C_{fn}} \quad (2)$$

If $\tan\delta_{el} \gg (1 + C_{fn}/C_{eln})$, $|V_{fn}|/|V_{tip}| \approx 1$. Approximately, the behavior of the ratio $|V_{fn}|/|V_{tip}|$ as a function of $\tan\delta_{el}$ can be described by the following argument (this is similar to the standard Bode plot analysis with $s = \tan\delta_{el}$ as the plot parameter). Below $\tan\delta_{el} \approx 1$, the ratio is approximately constant and equals the value defined by eq 2. At $\tan\delta_{el} \approx 1$, the ratio $|V_{fn}|/|V_{tip}|$ starts increasing quickly. The fast growth stops at $\tan\delta_{el} \approx (1 + C_{fn}/C_{eln})$, and after that, the ratio asymptotically approaches unity. The curve of the function will be S-shaped. The value of C_{fn}/C_{eln} is determined by dielectric constants of the film and electrolyte, film thickness, and the number of a partial circuit n, which is equivalent to the distance from the tip. Note that the ratio C_{fn}/C_{eln} is growing with increasing distance from the tip due to the conical tip shape and at sufficiently large distances $C_{fn} \gg C_{eln}$. This allows us to define a parameter, which we refer to as *localization length*, to characterize possible imaging resolution as a function of electrolyte conductivity and imaging frequency. For a given $\tan\delta_{el}$, one can find a partial circuit with a number n_0 such that

$$\frac{|V_{fn_0}|}{|V_{tip}|} = k\left(1 - \frac{C_{eln_0}}{C_{eln_0} + C_{fn_0}}\right) + \frac{C_{eln_0}}{C_{eln_0} + C_{fn_0}} \quad (3)$$

where k is a fraction of the whole swing of the ratio $|V_{fn}|/|V_{tip}|$ from its minimum value for n_0 at $\tan\delta_{el} = 0$, defined by eq 2, to unity. For $n < n_0$, the amplitude of the voltage drop across the film is close to voltage applied to the tip, and the localization effect of the tip is smeared out for these distances from the tip. The parameter $k < 1$ and its exact value can be set depending on the requirements of the experiment. In the case $C_{fn_0}/C_{eln_0} \gg \tan\delta_{el} \gg 1$, which is true for large enough distances from the tip, one can simplify the right-hand side of eq 1, and after substituting it in the left-hand side of eq 3 and following further simplification, one arrives at the equation for n_0:

$$\frac{C_{eln_0}}{C_{eln_0} + C_{fn_0}} = \frac{k}{\tan\delta_{el}} \quad (4)$$

We further note that an increase in the localization length with respect to the voltage drop across the film leads to a decrease of the peak value of the electric fields due to reduced potential gradients in the vicinity of the tip apex. This in turn results in decreased piezoresponse and signal strength in the PFM images.

While $\tan\delta_{el}$ can be readily determined from experimentally measured electrolyte conductivity, the dielectric constant, and a known driving frequency, the parameters C_{fn} and C_{eln} cannot be found experimentally or analytically. Therefore, we have performed

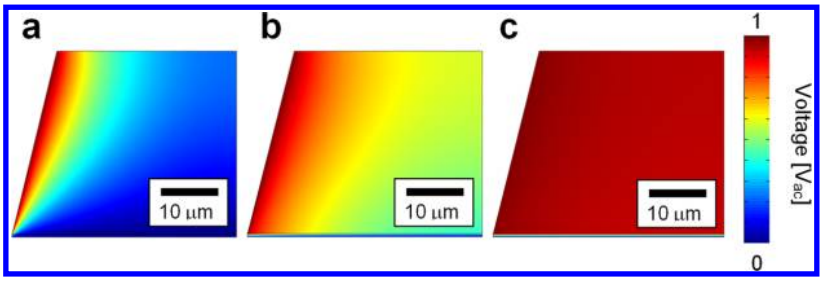

Figure 4. Numerically obtained voltage distributions when 1 V_{ac} is applied to the tip for the following electrolytes: (a) deionized water ($s = 1.5 \times 10^{-4}$ S/m, tan $\delta = 5.2 \times 10^{-2}$) and 10^{-4} M Na_2SO_4 solution ($s = 2.6 \times 10^{-3}$ S/m, tan $\delta = 0.9$); for these solutions, the potential distributions are indistinguishable at the length scale of the plot; (b) 10^{-2} M Na_2SO_4 solution ($s = 0.36$ S/m, tan $\delta = 124$); (c) 1 M Na_2SO_4 solution ($s = 1.73$S/m, tan $\delta = 590$).

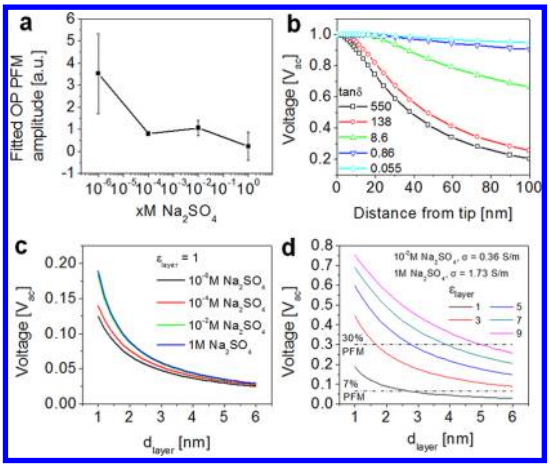

Figure 5. (a) OP PFM amplitude extracted from multifrequency detection methods as a function of molarity with a molarity of 10^{-6} for deionized water. (b) Voltage under the biased SPM tip as a function of radial distance for electrolytes with various tan δ when 1 V_{ac} is applied to the tip. (c) Effective voltage on the sample surface underneath the tip as a function of dead layer thickness, d_{layer}, for a dielectric constant of the dead layer of $\varepsilon_{layer} = 1$ for solutions of different conductivities. (d) Effective voltage on the sample surface underneath the tip as a function of dead layer thickness, d_{layer}, for 1 M Na_2SO_4 for various values of ε_{layer}. The effective voltages on the sample are indicated for 10^{-2} M Na_2SO_4 and 1 M Na_2SO_4 as estimated from (a) relative to the measurement in deionized water.

FE numerical modeling of the potential distribution across the electrolyte and the dielectric film. The simulations were performed using 2D axisymmetric models of the tip−sample system with an ac/dc module of COMSOL Multiphysics v.4.2 FE analysis package. Figures 4 and 5 depict the simulation result for different combinations of material parameters close to those used in the imaging experiments.

The series of plots in Figure 4a−c illustrates the delocalization of the stimulus from the probe tip with increasing conductivity of the electrolyte solutions. The FE model parameters used for the plots are as follows: film thickness is 500 nm, dielectric constants of electrolyte solutions and the film were 80 (water) and 107 (BFO),[33] respectively, and the driving frequency used was 650 kHz. Conductivity values for the electrolytes used in the simulations were obtained through measurements with a commercial conductivity meter. Note that for the lowest conductivity values corresponding to the DI water and to the 10^{-4} M Na_2SO_4 solution, when tan $\delta_{el} \lesssim 1$, the potential distributions are indistinguishable at the length scale of the plots, as can be expected from the predictions of the simple model of a chain of $C_{fn} + C_{eln} \| R_{eln}$ circuits.

DISCUSSION

In order to quantify the electromechanical response, several parameters need be known, independent of the measurement environment. Simplified, the surface displacement D is given by

$$D = X \cdot V_{applied} \cdot d_{eff} \cdot A(\omega) \cdot A_0 \qquad (5)$$

where $V_{applied}$ is the applied voltage to the tip, d_{eff} is the effective piezoelectric coefficient, $A(\omega)$ is the cantilever transfer function which is ideally 1 away from the contact resonance and Q at the resonance, and A_0 is the correlation between signal on the photodetector and actual displacement. Note that $V_{applied}$ is not necessarily the voltage acting at the surface of the sample since fields can be screened through adsorbate layers at the surface which is described by the screening factor X.

From Figure 2, it can be seen that the amplitude of the PFM signal decreases with increasing conductivity of the liquid solution. However, single frequency PFM close to the contact resonance peak can be subject to topography cross-talk, and SPM tips with different Q factors affect the measured PFM amplitude. Therefore, to extract the quantitative decrease of the electromechanical signal, contact resonance peaks are measured using the band excitation method (BE).[34] The PFM amplitude is extracted by fitting the contact resonance peak using a simple harmonic oscillator. This was done in a spatially resolved manner for a 256×256 grid in a $3 \times 3\ \mu m^2$ area. The averaged PFM amplitude for the imaged area is plotted as a function of molarity in Figure 5a.

According to the numerical simulations, the potential below the biased tip ($V_{applied}$) is not affected by the conductivity of the liquid, only the potential drop around the tip (Figure 5b). In addition, the parameters d_{eff}, A(ω), and A_0 do not change for liquids of different conductivity. Therefore, the decrease in PFM amplitude

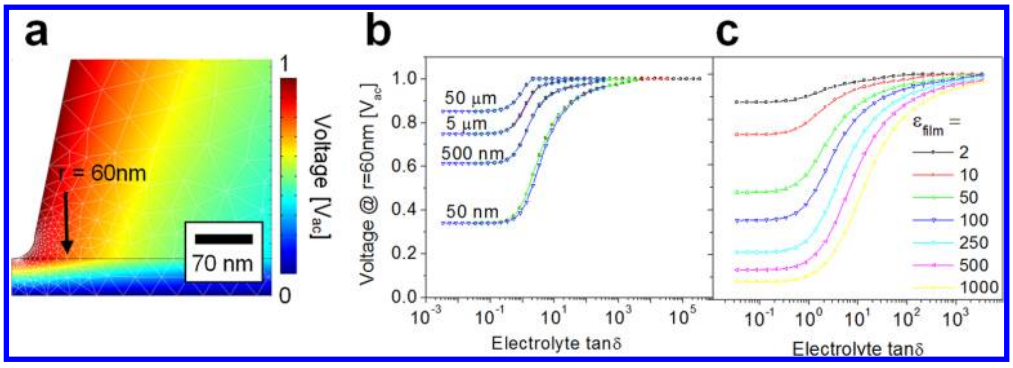

Figure 6. (a) Voltage distribution near the tip apex for an electrolyte tan δ = 14 and a film thickness 50 nm when 1 V_{ac} is applied to the tip. (b) Numerically obtained absolute values of the potential on the film surface at a distance from the tip r = 60 nm *vs* electrolyte loss tangent for film thicknesses, as indicated at the curves in the plot. The film dielectric constant is 107. The simulations were performed for four driving frequencies: 6.5 kHz (black), 65 kHz (red), 650 kHz (green), and 6.5 MHz (blue). Tip apex radius is 30 nm. (c) Absolute values of the potential on the film surface at a distance from the tip r = 60 nm *vs* electrolyte conductivity for a film thickness of 50 nm and different values of the film dielectric constant as indicated in the plot.

cannot be explained by the changes in electrical potential associated with the increase of electrolyte conductivity *per se*. Other factors influencing the PFM amplitude are the effective piezoelectric constant of the sample and the correlation between the photodetector signal and the actual sample expansion. Both parameters do not change with increasing conductivity of the liquid.

We argue that the decrease in PFM amplitude can be explained by the effect of the gap or low-permittivity "dead layer" between the tip and sample. We did not include a gap between the tip and sample in the simulation discussed above; however, in reality, such a "gap" is always present and is mainly formed by a low-polarizability layer of surface adsorbates on the sample and the tip. It is easily understandable that this effect is stronger at a higher ion concentration, resulting in a lower PFM amplitude.

From the changes of the PFM signal, which is directly proportional to the potential drop over the sample, the voltage on the sample surface can be estimated. This allows making some conclusion about the properties of the dead layer as described by the thickness d_{layer} and the dielectric constant ε_{layer}. We have modeled the voltage on the sample surface underneath the tip taking into account the presence of a dead layer. Figure 5c shows the voltage on the sample surface when a voltage of an 1 V_{ac} amplitude is applied to the tip as a function of the dead layer thickness under the assumption ε_{layer} = 1. The dead layer is assumed to be uniform across the whole sample surface. It can be seen that, in the presence of a dead layer, the voltage can drop significantly, and the voltage drop is stronger for larger d_{layer} and for solutions with lower conductivities. Note that the curves for 10^{-2} and 1 M Na_2SO_4 are nearly identical. For these molarities, the effective voltage drop across the sample can be experimentally estimated to be 30 and 7%, respectively, based of the changes in PFM amplitude relative to deionized water from Figure 5a. These values are plotted together with the effective voltage as a function of d_{layer} for various ε_{layer} values for 1 M (and 10^{-2} M) Na_2SO_4. It can be seen that a very low dielectric constant of around 1 is required to achieve the 7% PFM signal strengths for 1 M Na_2SO_4 if the dead layer thickness is around 2.7 nm. Higher values for ε_{layer} are possible, but then the dead layer thickness becomes unreasonably large. In the case of 10^{-2} M Na_2SO_4 with a 30% PFM amplitude, various combinations of ε_{layer} and d_{layer} can be found to explain the PFM amplitude drop and cannot be deconvoluted. If we assume that the thickness of the dead layer in this case cannot be larger than that for 1 M Na_2SO_4, then the dielectric constant of the dead layer needs to be below 5. Here, we are unable to extract any more information about the dead layer, and we have to refer to future experiments to uncover its nature and physical properties.

The localization length is another very important factor to be considered in electromechanical characterization. As shown above, depending on the conductivity of the electrolyte, the potential drop around the tip changes from localized to delocalized. This issue was also discussed by Rodriguez *et al.*[31] Despite the fact that the strain detection with the SPM tip will still be localized, a global field drop comes with some disadvantages. When the electromechanical effect of the sample is excited globally, the breakdown voltage of the sample or electrolyte is shifted to lower values due to the higher probability of influence of defects within the probed volume when compared to the local excitation scenario. Therefore, a local potential drop around the SPM tip is highly preferred.

For further considerations, we define the critical localization length as two times the tip radius, which is around 30 nm for the tip used in this study. If the electric potential at a distance from the tip r = 60 nm is small, the potential drop is local, if it is high, the potential drop is considered to be global (Figure 6a).

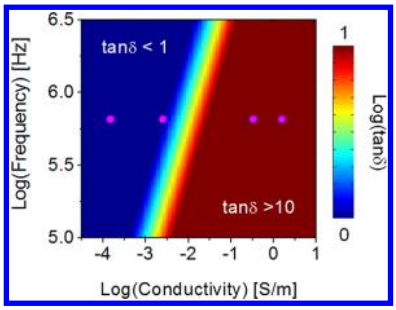

Figure 7. Logarithmic plot of tan δ as a function of measurement frequency and electrolyte conductivity as defined by tan $\delta = \sigma/\varepsilon\omega$. Blue areas are defined by tan $\delta < 1$, which represents a local sample excitation. Red areas display tan $\delta > 10$ when the potential drop around the tip becomes global. The pink dots represent the electrolytes and measurement frequency used in this study.

The numerical results strongly depend on the sample properties, such as sample thickness and dielectric properties. Figure 6 provides further elaboration of the numerically obtained tip−sample system behavior for the variation of these parameters. Figure 6b displays absolute values of the potential on the film surface at a distance from the tip r = 60 nm *versus* electrolyte loss tangent for four logarithmically spaced film thicknesses in the range of 50 nm to 5 μm. The plots are shown in a log−linear scale. We note that the behavior predicted by the simple lumped element model is clearly visible. Abs(V) as a function of tan δ_{el} first remains almost constant with increasing tan δ_{el} until a value tan $\delta_{el} \approx 1$, independent from the film's thickness. Afterward, it grows and comes to saturation asymptotically approaching unity. The value of tan δ_{el}, at which the saturation starts, decreases with increasing film thickness, as expected from the lumped element model. Note that, for a given distance from the tip, the ratio C_{fn}/C_{eln} drops with increasing film thickness. Identical behavior is observed for varying film dielectric constant, as evident from Figure 6c.

In most cases, the ionic conductivity of the electrolyte is a given parameter and cannot be modified easily without sacrificing functionality. In the following, different strategies are proposed to work in highly conductive electrolytes. One strategy is to use higher frequencies to excite the electromechanical effect, as evident from the definition of the loss tangent tan $\delta = \sigma/\varepsilon\omega$. In Figure 7, we provide a guideline plot, which shows the boundary between local and global field drop as af unction of measurement frequency and electrolyte conductivity based on the definition of the loss tangent. Here, we chose tan $\delta_{el} < 1$ as criteria for localized potential drop, as evident from Figure 6b for a BFO thin film of 50 nm (small electrical potential at r = 60 nm for tan $\delta_{el} < 1$). Figure 7 can be used to determine the measurement frequency for a given electrolyte conductivity to maintain a local potential drop. Since the contact resonance frequencies are fixed depending on the cantilever tip properties, higher eigenmodes have to be considered to be able to utilize higher frequencies or stiffer tips need to be used. Figure 7 also contains the conductivity points of the electrolyte used in this study. For the measurement frequency of 650 kHz, as used in Figure 2, one can see that the Na_2SO_4 solutions used span across the local to global potential scenarios.

A second strategy to further improve the potential localization is provided in Figure 6b. Evidently, thinner samples reduce the potential drop through the film at r = 60 nm, which illustrates that sample design can be utilized to facilitate potential localization and to enhance spatial resolution. However, this strategy is only possible if sample functionality can be maintained.

The data presented here were collected for BFO due to its relatively high dielectric constant of ~100, comparable to that of the electrolyte solvent, water ($\varepsilon_{H_2O} \approx 80$). The relative differences of the dielectric constants of the electrode and the electrolyte strongly affect the potential distribution around the tip, as is evident from Figure 6c. This is a very important point that has to be evaluated when other electromechanical systems are considered. A system of great interest is performing ESM on Li-ion battery materials, such as $LiCoO_2$, $LiMn_2O_4$, *etc.* in liquid electrolyte. Here, typical dielectric constants are between 15 and 20.[35] According to Figure 6c, this raises the potential at double the tip radius drastically for electrolytes with low conductivity, which corresponds to an increase of the localization length. This is a problem that needs to be considered carefully when samples with higher dielectric constants are considered and will be subject to future research.

CONCLUSION

In summary, an experimental and numerical study for the effect of electrolyte conductivity on nanoscale characterization of electromechanical phenomena in liquid is presented. $BiFeO_3$ and Na_2SO_4 were chosen as a model system for electromechanical phenomena and electrolytes, respectively. It was demonstrated that ferroelectric domains can be imaged up to 1 M Na_2SO_4 solutions; however, the resolution and signal strengths are reduced at these high concentrations. This is due to the fact that the potential drop around the biased SPM tip changes from locally to globally for electrolytes with increasing conductivity. It was demonstrated that a local potential drop is essential for nanoscale electromechanical characterization in liquid, and numerical simulation of the electric potential drop around the biased SPM tip as a function of sample properties outlines strategies to improve the potential localization for a given electrolyte conductivity. The identification of possible limitations and strategies is essential to develop advanced techniques for electromechanical measurements in liquids on a variety of sample systems, ranging from functional oxides to biological

samples. Only if these characterization techniques are in place, fundamental nanoscale phenomena and their role in macroscopic device functionality can be studied.

METHODS

The experiments were performed on 50 nm thick (001) oriented multiferroic BFO films with $SrRuO_3$ (SRO) bottom electrode epitaxially grown on low miscut (<0.01°) (001) $SrTiO_3$ (STO) single-crystal substrate by pulsed laser deposition as described elsewhere.[36] BFO is a well-characterized ferroelectric material with strong electromechanical responses with different out-of-plane and in-plane polarization components. PFM imaging was performed on a commercial SPM system (MFP-3D, Asylum Research) with metal-coated SPM tips (Nanosensors, k = 0.5−9.5 N/m). The Na_2SO_4 solutions were used in the form of a droplet on the sample surface as opposed to completely submerged samples to avoid electrical shorting between the tip and the sample ground, that is, the bottom electrode of the sample. OP and IP PFM contact resonance peaks were measured between 0 and 2 MHz, and the independent peaks for OP and IP PFM signals were identified.

Conflict of Interest: The authors declare no competing financial interest.

Acknowledgment. The experiments were designed and performed supported by the U.S. Department of Energy, Basic Energy Sciences, Materials Sciences and Engineering Division through the Office of Science Early Career Research Program. Instrumental capabilities and numerical calculations were provided and supported by the Center for Nanophase Materials Sciences, which is sponsored at Oak Ridge National Laboratory by the Scientific User Facilities Division, Office of Basic Energy Sciences, U.S. Department of Energy. Samples were provided through the collaboration with the National Chiao Tung University supported by the National Science Council under Contract No. NSC-101-2119-M-009-003-MY2, Ministry of Education under Grant No. MOE-ATU 101W961, and Center for Interdisciplinary Science of National Chiao Tung University.

REFERENCES AND NOTES

1. Cross, L. E. Ferroelectric Materials for Electromechanical Transducer Applications. *Mater. Chem. Phys.* **1996**, *43*, 108–115.
2. Park, S. E.; Shrout, T. R. Ultrahigh Strain and Piezoelectric Behavior in Relaxor Based Ferroelectric Single Crystals. *J. Appl. Phys.* **1997**, *82*, 1804–1811.
3. Nazri, G. A.; Pistoia, G. *Lithium Batteries: Science and Technology*; Springer Verlag: New York, 2009.
4. Adler, S. B. Factors Governing Oxygen Reduction in Solid Oxide Fuel Cell Cathodes. *Chem. Rev.* **2004**, *104*, 4791–4843.
5. Hantel, M. M.; Presser, V.; Kotz, R.; Gogotsi, Y. *In Situ* Electrochemical Dilatometry of Carbide-Derived Carbons. *Electrochem. Commun.* **2011**, *13*, 1221–1224.
6. Kepler, R. G.; Anderson, R. A. Ferroelectric Polymers. *Adv. Phys.* **1992**, *41*, 1–57.
7. Purvis, C. K.; Taylor, P. L. Piezoelectric and Pyroelectric Coefficients for Ferroelectric-Crystals with Polarizable Molecules. *Phys. Rev. B* **1982**, *26*, 4564–4570.
8. Kalinin, S. V.; Rodriguez, B. J.; Jesse, S.; Karapetian, E.; Mirman, B.; Eliseev, E. A.; Morozovska, A. N. Nanoscale Electromechanics of Ferroelectric and Biological Systems: A New Dimension in Scanning Probe Microscopy. In *Annual Review of Materials Research*; Annual Review: Palo Alto, CA, 2007; Vol. 37, pp 189−238.
9. Scott, J. F.; De Araujo, C. A. P. Ferroelectric Memories. *Science* **1989**, *246*, 1400–1405.
10. Polla, D. L.; Francis, L. F. Processing and Characterization of Piezoelectric Materials and Integration into Microelectromechanical Systems. *Annu. Rev. Mater. Sci.* **1998**, *28*, 563–597.
11. Gruverman, A.; Auciello, O.; Tokumoto, H. Scanning Force Microscopy for the Study of Domain Structure in Ferroelectric Thin Films. *J. Vac. Sci. Technol., B* **1996**, *14*, 602–605.
12. Harnagea, C.; Pignolet, A.; Alexe, M.; Satyalakshmi, K. M.; Hesse, D.; Gosele, U. Nanoscale Switching and Domain Structure of Ferroelectric $BaBi_4Ti_4O_{15}$ Thin Films. *Jpn. J. Appl. Phys. 2* **1999**, *38*, L1255–L1257.
13. Kalinin, S. V.; Bonnell, D. A. Imaging Mechanism of Piezoresponse Force Microscopy of Ferroelectric Surfaces. *Phys. Rev. B* **2002**, *65*, 125408.
14. Nath, R.; Chu, Y. H.; Polomoff, N. A.; Ramesh, R.; Huey, B. D. High Speed Piezoresponse Force Microscopy: <1 Frame per Second Nanoscale Imaging. *Appl. Phys. Lett.* **2008**, *93*, 072905.
15. Shvartsman, V. V.; Kholkin, A. L. Domain Structure of $0.8Pb(Mg_{1/3}Nb_{2/3})O_3-0.2PbTiO_3$ Studied by Piezoresponse Force Microscopy. *Phys. Rev. B* **2004**, *69*, 014102.
16. Ganpule, C. S.; Nagarajan, V.; Hill, B. K.; Roytburd, A. L.; Williams, E. D.; Ramesh, R.; Alpay, S. P.; Roelofs, A.; Waser, R.; Eng, L. M. Imaging Three-Dimensional Polarization in Epitaxial Polydomain Ferroelectric Thin Films. *J. Appl. Phys.* **2002**, *91*, 1477–1481.
17. Guyonnet, J.; Bea, H.; Guy, F.; Gariglio, S.; Fusil, S.; Bouzehouane, K.; Triscone, J. M.; Paruch, P. Shear Effects in Lateral Piezoresponse Force Microscopy at 180 Degrees Ferroelectric Domain Walls. *Appl. Phys. Lett.* **2009**, *95*, 132902.
18. Jungk, T.; Hoffmann, A.; Soergel, E. Quantitative Analysis of Ferroelectric Domain Imaging with Piezoresponse Force Microscopy. *Appl. Phys. Lett.* **2006**, *89*, 163507.
19. Roelofs, A.; Bottger, U.; Waser, R.; Schlaphof, F.; Trogisch, S.; Eng, L. M. Differentiating 180 Degrees and 90 Degrees Switching of Ferroelectric Domains with Three-Dimensional Piezoresponse Force Microscopy. *Appl. Phys. Lett.* **2000**, *77*, 3444–3446.
20. Takashima, K.; Horie, S.; Mukai, T.; Ishida, K.; Matsushige, K. Piezoelectric Properties of Vinylidene Fluoride Oligomer for Use in Medical Tactile Sensor Applications. *Sens. Actuators, A* **2008**, *144*, 90–96.
21. Sharma, P.; Reece, T. J.; Ducharme, S.; Gruverman, A. High-Resolution Studies of Domain Switching Behavior in Nanostructured Ferroelectric Polymers. *Nano Lett.* **2011**, *11*, 1970–1975.
22. Gruverman, A.; Wu, D.; Rodriguez, B. J.; Kalinin, S. V.; Habelitz, S. High-Resolution Imaging of Proteins in Human Teeth by Scanning Probe Microscopy. *Biochem. Biophys. Res. Commun.* **2007**, *352*, 142–146.
23. Rodriguez, B. J.; Kalinin, S. V.; Shin, J.; Jesse, S.; Grichko, V.; Thundat, T.; Baddorf, A. P.; Gruverman, A. Electromechanical Imaging of Biomaterials by Scanning Probe Microscopy. *J. Struct. Biol.* **2006**, *153*, 151–159.
24. Kholkin, A.; Amdursky, N.; Bdikin, I.; Gazit, E.; Rosenman, G. Strong Piezoelectricity in Bioinspired Peptide Nanotubes. *ACS Nano* **2010**, *4*, 610–614.
25. Liu, Y. M.; Zhang, Y. H.; Chow, M. J.; Chen, Q. N.; Li, J. Y. Biological Ferroelectricity Uncovered in Aortic Walls by Piezoresponse Force Microscopy. *Phys. Rev. Lett.* **2012**, *108*, 078103.
26. Amatucci, G. G.; Tarascon, J. M.; Klein, L. C. CoO_2, the End Member of the Li_xCoO_2 Solid Solution. *J. Electrochem. Soc.* **1996**, *143*, 1114–1123.
27. Balke, N.; Jesse, S.; Kim, Y.; Adamczyk, L.; Tselev, A.; Ivanov, I. N.; Dudney, N. J.; Kalinin, S. V. Real Space Mapping of Li-Ion Transport in Amorphous Si Anodes with Nanometer Resolution. *Nano Lett.* **2010**, *10*, 3420–3425.
28. Balke, N.; Jesse, S.; Morozovska, A. N.; Eliseev, E.; Chung, D. W.; Kim, Y.; Adamczyk, L.; Garcia, R. E.; Dudney, N.;

Kalinin, S. V. Nanoscale Mapping of Ion Diffusion in a Lithium-Ion Battery Cathode. *Nat. Nanotechnol.* **2010**, *5*, 749–754.
29. Balke, N.; Jesse, S.; Chu, Y.-H.; Kalinin, S. V. High-Frequency Electromechanical Imaging of Ferroelectrics in a Liquid Environment. *ACS Nano* **2012**, *6*, 5559–5565.
30. Rodriguez, B. J.; Jesse, S.; Baddorf, A. P.; Kalinin, S. V. High Resolution Electromechanical Imaging of Ferroelectric Materials in a Liquid Environment by Piezoresponse Force Microscopy. *Phys. Rev. Lett.* **2006**, *96*, 237602.
31. Rodriguez, B. J.; Jesse, S.; Baddorf, A. P.; Kim, S. H.; Kalinin, S. V. Controlling Polarization Dynamics in a Liquid Environment: From Localized to Macroscopic Switching in Ferroelectrics. *Phys. Rev. Lett.* **2007**, *98*, 247603.
32. Rodriguez, B. J.; Jesse, S.; Habelitz, S.; Proksch, R.; Kalinin, S. V. Intermittent Contact Mode Piezoresponse Force Microscopy in a Liquid Environment. *Nanotechnology* **2009**, *20*, 195701.
33. Palkar, V. R.; John, J.; Pinto, R. Observation of Saturated Polarization and Dielectric Anomaly in Magnetoelectric $BiFeO_3$ Thin Films. *Appl. Phys. Lett.* **2002**, *80*, 1628–1630.
34. Jesse, S.; Kalinin, S. V.; Proksch, R.; Baddorf, A. P.; Rodriguez, B. J. The Band Excitation Method in Scanning Probe Microscopy for Rapid Mapping of Energy Dissipation on the Nanoscale. *Nanotechnology* **2007**, *18*, 435503.
35. Hart, F. X.; Bates, J. B. Lattice Model Calculation of the Strain Energy Density and Other Properties of Crystalline $LiCoO_2$. *J. Appl. Phys.* **1998**, *83*, 7560–7566.
36. Balke, N.; Choudhury, S.; Jesse, S.; Huijben, M.; Chu, Y. H.; Baddorf, A. P.; Chen, L. Q.; Ramesh, R.; Kalinin, S. V. Deterministic Control of Ferroelastic Switching in Multiferroic Materials. *Nat. Nanotechnol.* **2009**, *4*, 868–875.